IOP Publishing Nanotechnology
Nanotechnology 30 (2019) 275302 (10pp) https://doi.org/10.1088/1361-6528/ab11ad

Layer-by-layer thinning of MoS_2 via laser irradiation

Bien-Cuong Tran-Khac[1], Ryan M White[2], Frank W DelRio[2] and Koo-Hyun Chung[1]

[1] School of Mechanical Engineering, University of Ulsan, Ulsan 44610, Republic of Korea
[2] Applied Chemicals and Materials Division, Material Measurement Laboratory, National Institute of Standards and Technology, Boulder, CO 80305, United States of America

E-mail: khchung@ulsan.ac.kr

Received 9 January 2019, revised 12 March 2019
Accepted for publication 20 March 2019
Published 17 April 2019

Abstract

Layer-by-layer thinning of molybdenum disulfide (MoS_2) via laser irradiation was examined using Raman spectroscopy and atomic force microscopy. In particular, the effects of number of layers, laser conditions, and substrate were systematically identified. The results demonstrated the presence of nanoparticles on the MoS_2 at sufficient laser treatment conditions prior to layer-by-layer thinning. The volume of nanoparticles was found to increase and then decrease as the number of MoS_2 layers increased; the non-monotonic trend was ascribed to changes in the thermal conductivity of the film and interfacial thermal conductance between the film and substrate with number of layers. Moreover, the volume of nanoparticles was found to increase as the magnification of the objective lens decreased and as laser power and exposure time increased, which was attributed to changes in the power density with laser conditions. The effect of substrate on nanoparticle formation and layer-by-layer thinning was investigated through a comparison of freestanding and substrate-supported MoS_2 subjected to laser irradiation; it was illustrated that freestanding films were thinned at lower laser powers than substrate-supported films, which highlighted the function of the substrate as a heat sink. For conditions that elicited thinning, it was shown that the thinned areas exhibited triangular shapes, which suggested anisotropic etching behavior where the lattice of the basal plane was preferentially thinned along the zigzag direction terminated by an Mo- or S-edge. High-resolution transmission electron microscopy of freestanding MoS_2 revealed the presence of a 2 nm thick amorphous region around the laser-treated region, which suggested that the crystalline structure of laser-treated MoS_2 remained largely intact after the thinning process. In all, the conclusions from this work provide useful insight into the progression of laser thinning of MoS_2, thereby enabling more effective methods for the development of MoS_2 devices via laser irradiation.

Keywords: atomic force microscopy, layer-by-layer thinning, molybdenum disulfide, nanoparticles, laser irradiation

(Some figures may appear in colour only in the online journal)

1. Introduction

Transition metal dichalcogenides have received considerable interest in recent history [1–4]. In particular, atomically-thin MoS_2 has been extensively studied due to its unique electrical, mechanical, frictional, and optical properties [5–7]. Based on these properties, atomically-thin MoS_2 has been vital in the development of next-generation electronics and optoelectronics [8]; electrochemical energy storage [9]; therapeutic, bioimaging, and biosensing [10]; and environmental [11] applications. In electronics and optoelectronics, the structure, symmetry, and thickness-dependent evolution of the electronic and phononic structure have facilitated advancements in field-effect transistors [12], heterostructure junctions [13], photodetectors [14], photovoltaic cells [15], and gas sensors [16]. In energy storage, the relationship between morphology and electrochemical

performance in MoS_2-based nanocomposites enabled novel solutions with high capacities and stable cycle performances for lithium ion batteries [17], sodium ion batteries [18], and supercapacitors [19]. Similarly, MoS_2-based nanomaterials have exhibited promise in therapeutic and diagnostic modalities such as photothermal therapy [20], drug delivery [21], gene therapy [22], and biosensing [23]. Moreover, adsorption, photodegradation, semiconducting, and antifouling capabilities have resulted in environmental benefits previously unattainable in two-dimensional (2D) materials, leading to water-related functions for contaminant adsorption [24], photocatalysis [25], membrane-based separation [26], and disinfection [27]. These seemingly incongruent areas are connected by a common theme—the tunability of the underlying properties is often brought about by discrete changes to the atomically-thin MoS_2 thickness. Therefore, to use atomically-thin MoS_2 to its full potential in micro- and nanoscale devices and extend its usage into other applications, methods to obtain high-quality MoS_2 with controllable shape, size, and thickness are required.

Several top-down and bottom-up methods have been developed to fabricate atomically-thin MoS_2. The top-down methodologies include mechanical [28] and solution-based [29] exfoliation. The former approach produces high-quality atomically-thin MoS_2, but suffers from low yield and reproducibility, while the latter method enables improved yield, but at the expense of residual chemicals from the solution [30]. In contrast, bottom-up methods have been established via chemical vapor deposition (CVD) [31]. CVD has shown the ability to produce large-area atomically-thin MoS_2 with similar or superior properties to exfoliated methods, but the resulting samples often require a substrate transfer to enable the specific application area. In all, it is clear that significant progress has been made in the quest to fabricate high-quality MoS_2, but that more work is required to improve on the deficiencies described above and to enable MoS_2 with controllable shape, size, and thickness. To this end, more recent work has focused on layer-by-layer thinning of MoS_2. One approach involved thermal annealing of MoS_2 in air [32] and argon [33]; in both cases, the MoS_2 was peeled layer-by-layer and the remaining layers exhibited similar structure and properties, but stopped short of using the approach to dictate lateral dimensions. Such control over lateral dimensions was achieved using argon plasma [34] and XeF_2 gas [35] with standard lithographic techniques to generate 2D heterostructures with alternating MoS_2 layer thicknesses. Another fabrication method for obtaining such MoS_2 features was based on layer-by-layer thinning via laser irradiation [36]. Recent studies have shown that atomically-thin MoS_2 with different thicknesses and surface patterns can be obtained from laser thinning [37, 38]. The properties of laser-thinned monolayers were found to be comparable to those of pristine MoS_2 single layers [36, 37], thereby providing a viable path towards the fabrication of three-dimensional devices [38]. Despite the recent success, however, there are still several aspects of the laser thinning process that are not yet fully understood. For instance, recent reports have shown that nanoparticles are formed on the laser-treated areas, which have tentatively been attributed to the oxidation, etching, and redeposition of MoS_2 [39, 40]. Also, it is uncertain if the temperature increase from laser irradiation has deleterious effects on the structure of the surrounding MoS_2 [41]. As such, more detailed and systematic studies are needed to completely elucidate the effects of the laser irradiation process on MoS_2.

In this work, layer-by-layer thinning of MoS_2 via laser irradiation is studied using Raman spectroscopy and atomic force microscopy. In more detail, the effects of number of layers, laser conditions, and substrate on nanoparticle formation and thinning characteristics are identified. For number of layers, the volume of nanoparticles and thinning behavior are characterized as a function of MoS_2 thickness; the observed trends are explained via changes to the thermal behavior of the film and substrate. For laser conditions, the volume of nanoparticles and thinning behavior are studied for different objective lens magnifications, laser powers, and exposure times and interpreted through the associated changes in the laser power density. For substrate, both substrate-supported and freestanding specimens are examined and the differences in thinning rates are explained by the changes to the heat dissipation mechanisms. Finally, transmission electron microscopy is used to assess the crystalline structure of the MoS_2 away from and next to the laser-treated regions, thereby enabling a mechanistic understanding of the etch process in the in-plane and through-thickness directions.

2. Materials and methods

Atomically-thin and bulk MoS_2 were produced from single-crystal MoS_2 (SPI) using the micromechanical exfoliation method. The specimens were repeatedly exfoliated from the bulk crystal using an adhesive tape. The exfoliated specimens were gently pressed against and transferred to an SiO_2/Si substrate; in previous work, the roughness of single-layer MoS_2 was found to be close to that of the SiO_2/Si substrate, suggesting good flexibility and conformity to the underlying substrate [42, 43]. The thickness of the thermally-grown SiO_2 layer on the Si substrate was ≈300 nm. Optical microscopy (VK-X200, Keyence), atomic force microscopy (AFM) (MFP-3D, Asylum Research), and Raman spectroscopy (Alpha300R, Witec) were employed to examine the topographies and thicknesses of the specimens prior to the laser treatments. In detail, after identification of locations of the specimens using optical microscopy, topographic images were obtained with intermittent-contact mode AFM using Si probes with a nominal normal spring constant of 2 N m^{-1} (AC240, Olympus). Raman spectroscopy measurements were performed using an excitation laser wavelength of 532 nm. The Raman spectra were collected through a 100× objective (NA ≈ 0.9) with a laser spot size of about 720 nm, and the spectra resolution was set to be about 1.4 cm^{-1} (1800 lines mm^{-1} grating). The laser power was kept below 0.5 mW with an acquisition time of 10 s to avoid laser-induced thermal effects and nanoparticle formation on the specimens [39].

The laser thinning process of MoS_2 was then systematically investigated with Raman spectroscopy and AFM

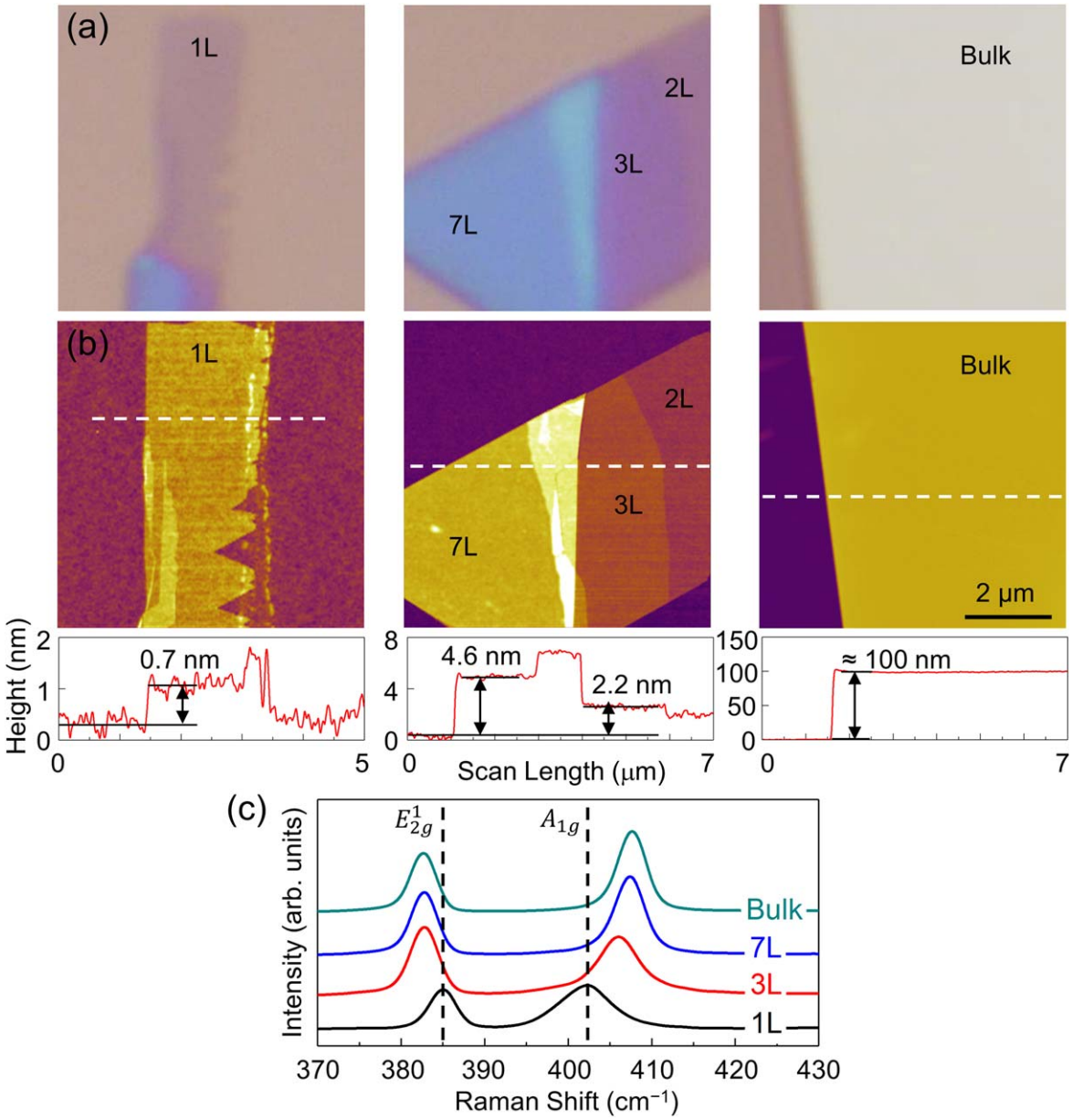

Figure 1. (a) Optical microscopy images, (b) AFM topographic images with cross-sectional height profiles, and (c) Raman spectra for 1L, 3L, 7L, and bulk MoS_2 specimens on an SiO_2 substrate. The white dashed lines in (b) denote the locations where the cross-sectional height profiles were taken. The black dashed lines in (c) denote the Raman characteristic peak positions for 1L MoS_2.

measurements. The laser treatments were achieved using the 532 nm continuous-wave laser with a given objective lens, laser power, and exposure time after identifying one-layer (1L), three-layer (3L), seven-layer (7L), and bulk MoS_2 flakes and focusing the Raman laser spot on the specimen surfaces. Two different Raman objective lenses were used in this work, including the 50× (Nikon) (NA ≈ 0.8) and 100× (NA ≈ 0.9) objective lens; the working distances of the 50× (NA ≈ 0.8) and 100× (NA ≈ 0.9) lenses were estimated to be about 0.54 and 1.0 mm, respectively. For the laser power experiments, the power varied from 10 to 40 mW for a constant exposure time of 60 s, while for the exposure time experiments, the time ranged from 10 to 100 s at a constant laser power of 25 mW. All Raman and AFM measurements were conducted in ambient conditions (25 °C, 40% RH).

The laser thinning process was also investigated with high-resolution transmission electron microscopy (TEM). The goals of the TEM study were two-fold: (1) to examine the effects of substrate on nanoparticle formation and laser thinning and (2) to examine the shape and crystalline structure of laser-treated regions. To this end, an MoS_2 specimen was deposited onto a TEM Cu grid (Pelco, Ted Pella). The thickness of this free-standing MoS_2 specimen was determined to be about 480 nm via AFM. The freestanding specimen was then exposed to laser powers ranging from 10 to 20 mW for 60 s and imaged at atomic resolution with a JEOL ARM 200F aberration corrected scanning transmission microscope at 200 keV. The convergence angle was 22.7 mrad and the collection angle (HAADF detector) was in the range of 90 to 370 mrad. The microscope was focused and aligned away from the areas of interest to prevent beam damage.

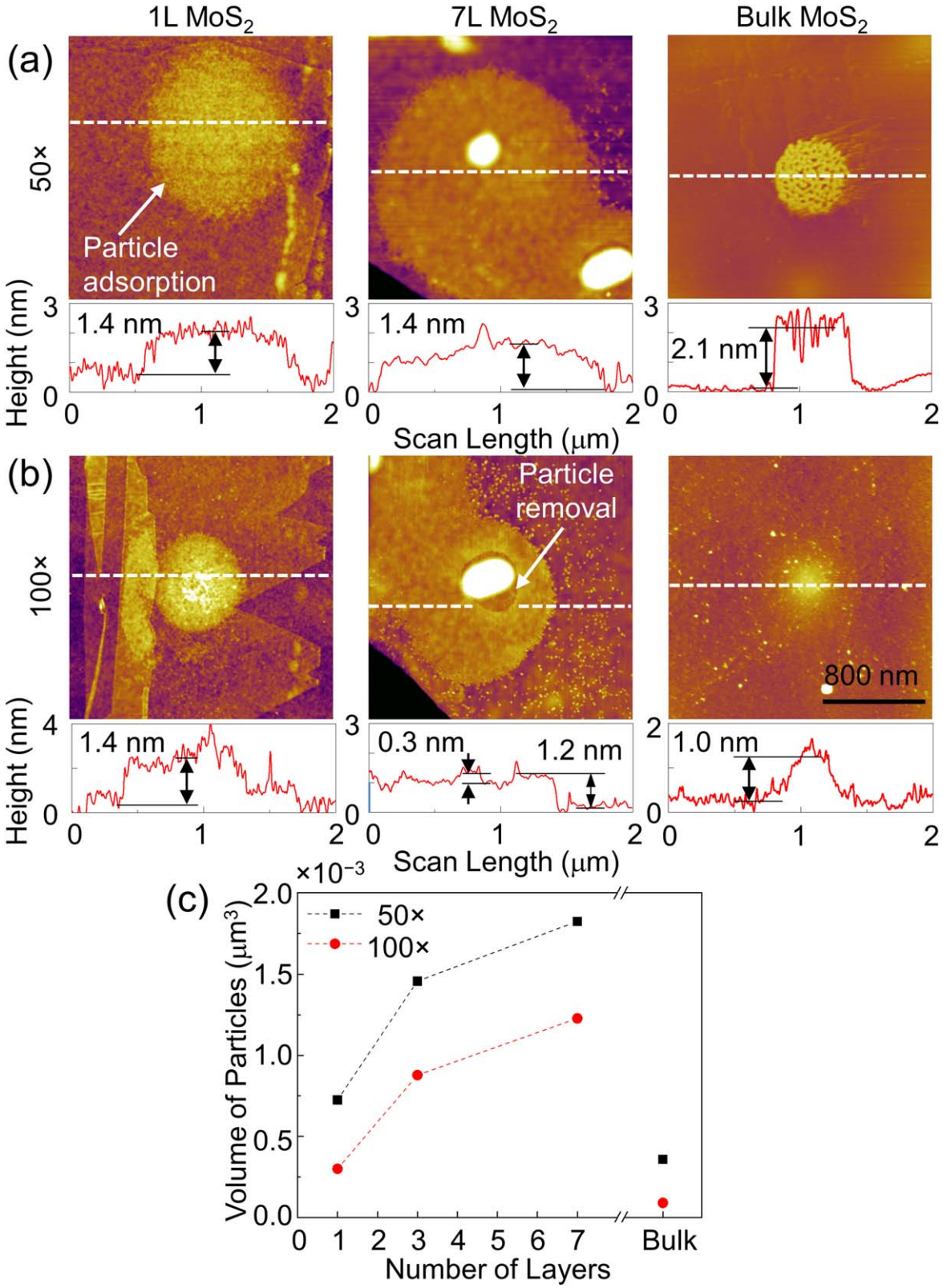

Figure 2. AFM topographic images and cross-sectional height profiles of 1L, 7L, and bulk MoS_2 specimens after laser treatments with (a) 50× and (b) 100× objective lenses at 5 mW for 60 s. (c) Nanoparticle volume as a function of number of layers and objective lens magnification. The white dashed lines in (a) and (b) denote the locations where the cross-sectional height profiles were taken.

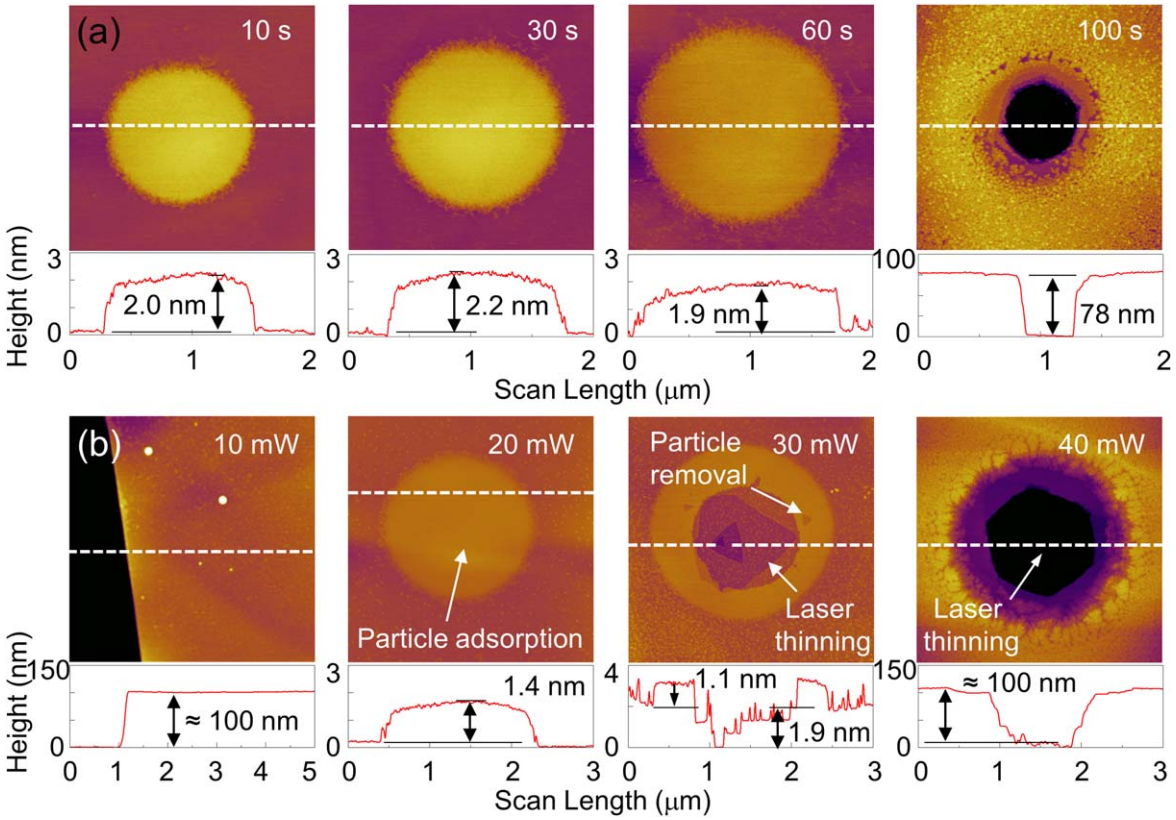

Figure 3. AFM topographic images and cross-sectional height profiles of bulk MoS_2 specimens after laser treatments with a 100× objective lens at (a) 25 mW for 10 to 100 s and (b) 10 to 40 mW for 60 s. The white dashed lines in (a) and (b) denote the locations where the cross-sectional height profiles were taken.

3. Results

Figure 1(a) shows optical microscopy images of 1L, 3L, 7L, and bulk MoS_2 specimens on an SiO_2 substrate. AFM topographic images of the MoS_2 specimens are shown in figure 1(b). The images clearly indicate that the specimen surfaces were initially clean and particle-free. From the cross-sectional height profiles in figure 1(b), it was also determined that the thicknesses of the as-deposited specimens were about 0.7, 2.2 and 4.6 nm, which correspond to those of 1L, 3L, and 7L MoS_2 (assuming a theoretical thickness of 0.62 nm for 1 L MoS_2). In addition, it was observed that the thickness of the bulk MoS_2 specimen was ≈100 nm. Raman spectra of the MoS_2 specimens are also provided in figure 1(c), which clearly reveal a dependence of Raman characteristic peak position on thickness. As the number of layers increased, the E^1_{2g} peak frequency from in-plane vibrations of Mo-S atoms decreased and the A_{1g} peak frequency from out-of-plane vibrations of S atoms increased, in agreement with previous work [44].

Figure 2 shows AFM topographic images and cross-sectional height profiles of 1L, 7L, and bulk MoS_2 specimens after laser treatments with 50× and 100× objective lenses at 5 mW for 60 s. In all cases, the data clearly show the formation of nanoparticles on the top surfaces after the laser treatment process; in previous work, the nanoparticles were attributed to oxidation, etching, and redeposition of MoS_2 [40]. However, it is demonstrated here that the extent of nanoparticle formation is highly dependent on (1) the MoS_2 thickness and (2) objective lens magnification. On point (1), the volume of nanoparticles was found to increase and then decrease with number of layers as shown in figure 2(c); the non-monotonic trend was ascribed to changes in thermal conductivity of the film and interfacial thermal conductance between the film and substrate with number of layers [39]. For atomically-thin MoS_2, the interfacial thermal conductance is the dominant heat transfer mechanism. As the number of layers increases, interfacial heat transfer decreases and in-plane heat transfer increases, which results in an increase in nanoparticle volume. In contrast, the thermal conductivity of the film is the dominant heat transfer mechanism for bulk MoS_2. The local heat from the laser dissipates more effectively in the lateral direction due to the greater thermal conductivity for bulk MoS_2 than that for atomically-thin MoS_2, which leads to a decrease in nanoparticle volume and the non-monotonic trend. Interestingly, the 7L specimens exhibited the largest nanoparticle volume and the only indication of laser thinning at this power (a height decrease of ≈0.3 nm), suggesting that nanoparticle formation is a precursor to thinning. On point (2), the nanoparticle volume was found to increase as the objective lens magnification decreased as shown in figure 2(c). Moreover, thinning was only observed with the 100× lens, as previously noted. The differences in nanoparticle volume and laser thinning were due to differences in laser spot size, which were ≈810 nm and 720 nm for

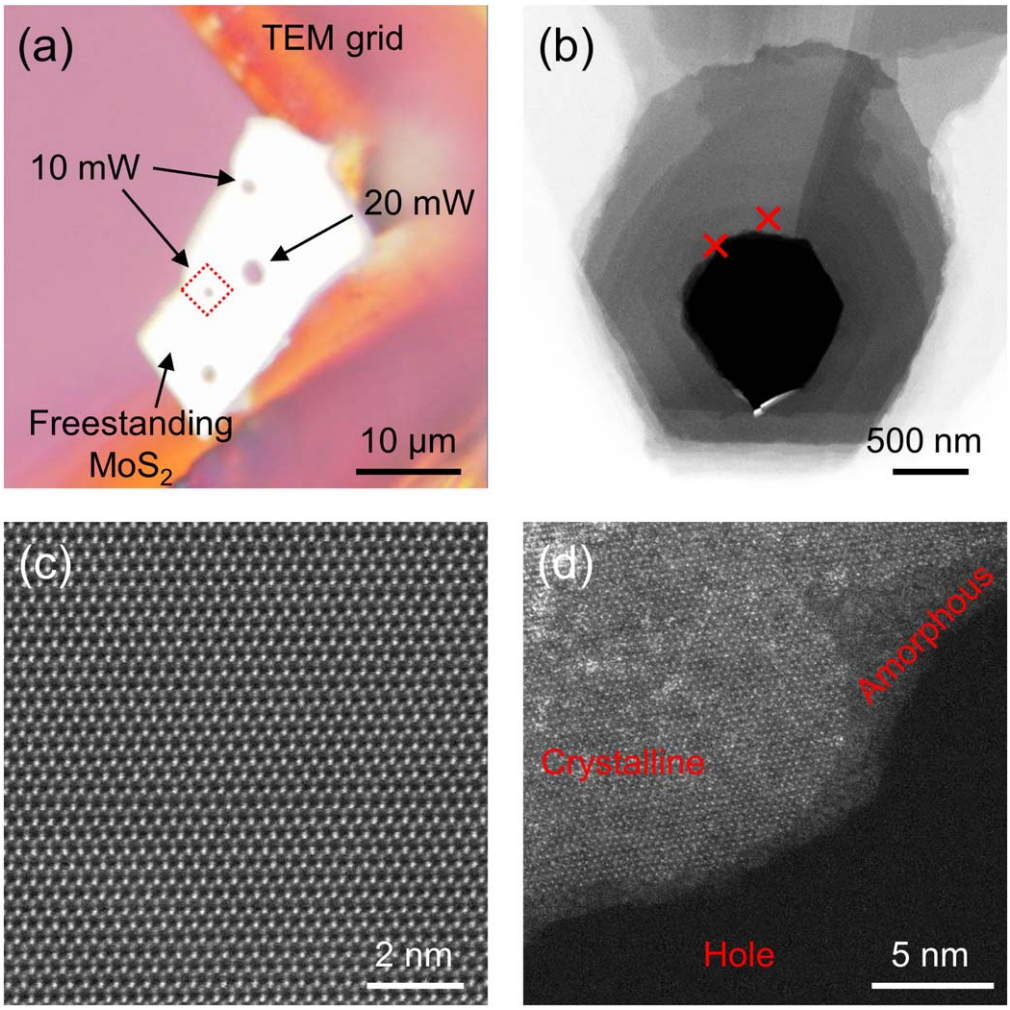

Figure 4. (a) Optical microscopy image of a freestanding MoS_2 specimen after laser treatment with a 100× objective lens at 10 and 20 mW for 60 s. (b) Low-resolution TEM image of the 10 mW laser-treated region. High-resolution TEM images of the 10 mW laser-treated region (c) away from and (d) next to the hole. The red square in (a) denotes the location where the low-resolution TEM image was taken. The red marks in (b) denote the locations where the high-resolution TEM images were taken.

the 50× and 100× lenses, respectively. The larger spot size for the 50× lens translated to a larger nanoparticle area (and hence volume), whereas the smaller spot size for the 100× lens allowed for a larger power density and higher temperature at the treated area (and hence thinning) [45]. Moreover, given that the onset of etching was witnessed for 7L MoS_2 with the 100× lens at 5 mW for 60 s, it is likely that only a slight increase to power or time would be required to observe the same behavior with the 50× lens.

Figure 3(a) shows AFM topographic images and cross-sectional height profiles of bulk MoS_2 after laser treatments at 25 mW for exposure times from 10 to 100 s. As the exposure time increased, the nanoparticle volume also increased, until laser thinning was finally observed at 100 s. Assuming a Gaussian distribution for the laser intensity profile [45], it is likely that the surface temperature reached a maximum at the center of the treated area and decreased radially outward, which explains the non-uniform height distributions. In addition, it was found that the nanoparticle height remained relatively constant (1.9 to 2.2 nm), but that the nanoparticle area increased significantly, as the exposure time increased. This suggests that the through-thickness heat transfer becomes saturated, but that the in-plane heat transfer continues to increase with time, which again highlights that the thermal conductivity is the dominant heat transfer mechanism for bulk MoS_2. Figure 3(b) shows AFM topographic images and height profiles of bulk MoS_2 after laser treatments for 60 s at powers from 10 to 40 mW. No significant change in topography was observed at 10 mW. However, at 20 mW, laser-induced nanoparticle formation was observed, but with no significant thinning of the MoS_2 layers. At 30 mW, up to three layers of MoS_2 (≈1.9 nm) were removed, as evident from the cross-sectional profiles. Interestingly, the shape of the thinned area at the center of the laser-treated area was triangular, in contrast to the circular shape of the nanoparticles removed from the center of the thinned area. In addition, it was observed that the orientation of the triangular pattern on the second top layer was 180° different than that on the top layer, but in alignment with that on the third layer. At 40 mW, >150 layers of MoS_2 (≈100 nm) were thinned from

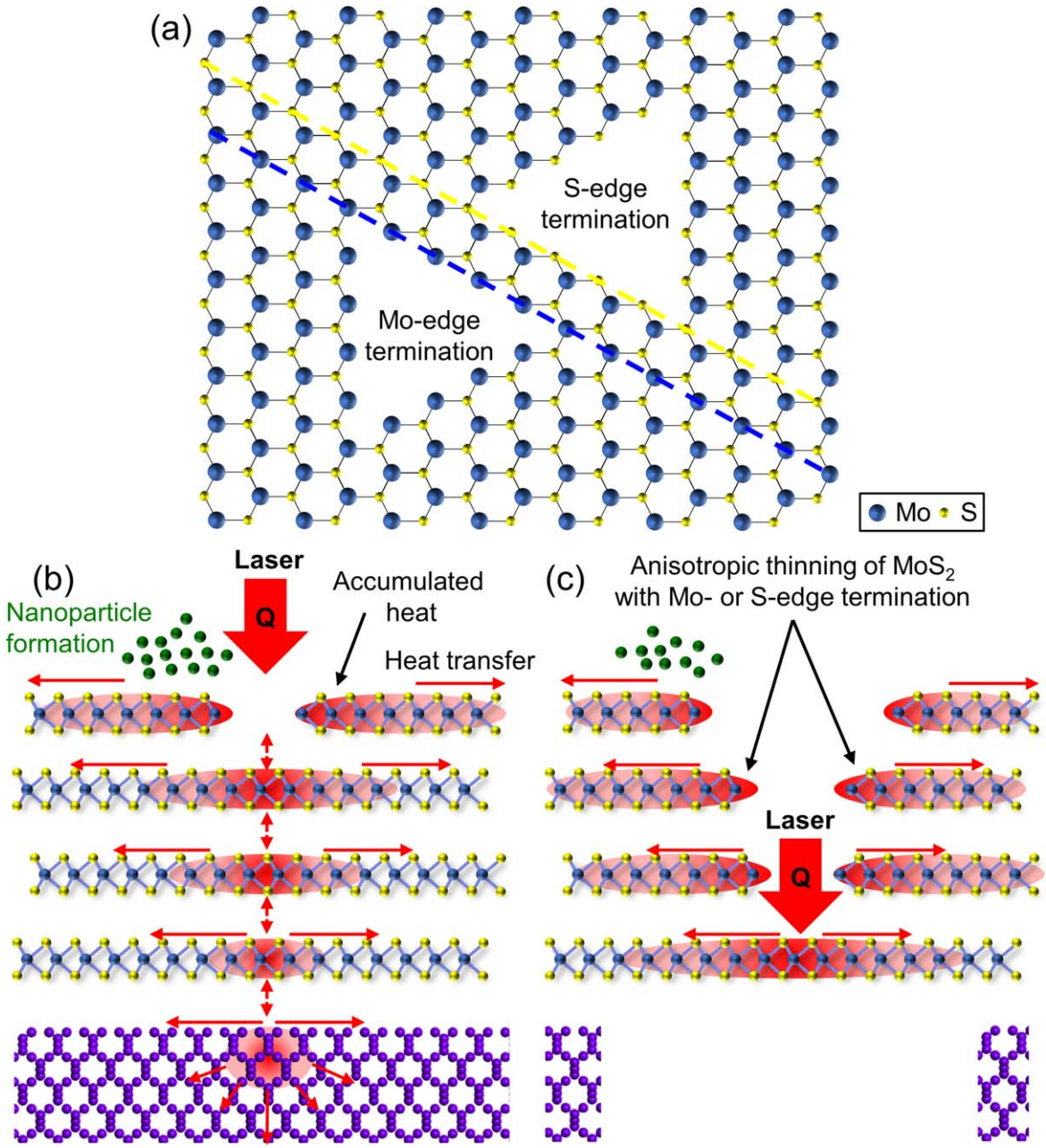

Figure 5. Schematic diagrams of the MoS_2 thinning process in the (a) in-plane and (b)–(c) through-thickness directions. The blue and yellow dashed lines in (a) represent the Mo and S edges, respectively. The green circles and red arrows in (b) and (c) denote the nanoparticles on the top surface and main heat transfer paths through the film and substrate, respectively.

the laser treatment. In this case, the thinned area retained a hexagonal shape, which was likely formed from multiple triangular patterns as etching progressed through the layers.

Figure 4 shows the optical microscopy and TEM images of the freestanding specimen on the TEM grid after laser treatments at 10 and 20 mW for 60 s. At both powers, thinning through the entire specimen was observed. The diameter of the hole for 20 mW was larger than that for 10 mW, but both holes exhibited hexagonal shapes as with the substrate-supported films. In contrast, the thinning rates for the freestanding and substrate-supported films were vastly different. For example, at 10 mW, the substrate-supported MoS_2 exhibited no nanoparticle formation or laser thinning, while the freestanding MoS_2 was completely thinned. High-resolution TEM was utilized to assess the crystalline structure of the MoS_2 away from and next to the laser-treated regions; the locations are denoted in figure 4(b). Away from the region, the MoS_2 demonstrated a defect-free hexagonal structure, with a fringe lattice spacing of 0.27 nm indicative of the (100) plane. In contrast, the MoS_2 exhibited a 2 nm thick amorphous region around the laser-treated region, most likely an artifact of the irradiation process and a precursor to layer-by-layer thinning. An amorphous region of similar thickness was also observed at 20 mW, suggesting the presence and size of

the layer is invariant with laser power. This confirms that laser thinning can be used to create devices with pristine layers, given that the crystalline structure remains largely intact.

4. Discussion

The systematic investigation of MoS_2 laser thinning presented herein enables a mechanistic understanding of the etching process. The results demonstrate the presence of nanoparticles on the MoS_2 at sufficient laser treatment conditions prior to layer-by-layer thinning; previous work submits that the nanoparticles are due to the oxidation, etching, and redeposition of the MoS_2 [39, 40]. It is hypothesized here that the nanoparticles act as nucleation sites for the subsequent layer-by-layer thinning. The schematic diagrams in figure 5 illustrate the thinning process in both the in-plane and through-thickness directions. In figure 5(a), it is shown that the thinned areas exhibit triangular shapes, which suggests anisotropic etching behavior where the lattice of the basal plane is preferentially thinned along a zigzag direction terminated by an Mo- or S-edge depending on stability. Determination of the more stable edge termination here is complicated, given its dependence on sulfiding conditions, chemical environment, and substrate [46–48]. The formation of triangular pits on an MoS_2 surface was also observed in a previous study [41], in which the atomically-thin MoS_2 was thermally annealed from 300 °C to 340 °C in an oxygen environment. It should also be noted that the changes in the orientations of the triangular patterns could be accredited to trigonal prismatic crystal structures such as the 2H- and 3R-phases for MoS_2. Particularly, for the trigonal prismatic coordination, 2H-MoS_2 consists of two layers of MoS_2 per unit cell stack in the hexagonal symmetry, while 3R-MoS_2 has three layers of MoS_2 per unit cell stack in the rhombohedral symmetry [49]. Therefore, the 180° rotation of the triangular lattices for adjacent layers in figure 3(b) is indicative of the 2H-MoS_2 and not the 3R-MoS_2 phase [50, 51]. In general, the 2H-phase is more stable and dominant in nature [52], providing further evidence for its presence here. Interestingly, the triangular orientations on the second and third layers are similar, which suggests that the stacking order is a hybrid of the 2H-MoS_2 and 3R-MoS_2 phases [53]. In figures 5(b) and (c), the effect of the substrate on thinning rate is highlighted. For substrate-supported MoS_2, the laser-induced heat is readily dissipated from the laser-treated area through the MoS_2 layers to the substrate, which acts as a heat sink. Hence, the substrate can prevent or delay the occurrence of laser thinning, depending on the laser conditions. In contrast, heat accumulates at the laser-treated area in the free-standing MoS_2, enabling a faster thinning rate. This finding is in agreement with results from previous studies [36, 54] and opens the door to patterned substrates with variable thermal properties to enable three-dimensional MoS_2 devices.

5. Conclusions

In summary, layer-by-layer thinning of MoS_2 via laser irradiation was investigated via Raman spectroscopy, AFM, and TEM on substrate-supported and freestanding specimens. In all cases, the results clearly showed the formation of nanoparticles on the top surfaces after the laser treatment process; previous work attributed the nanoparticles to oxidation, etching, and redeposition of MoS_2 [40]. The extent of nanoparticle formation was highly dependent on the number of layers, laser conditions, and substrate. For conditions that elicited thinning, the thinned areas exhibited triangular shapes, which suggests anisotropic etching behavior where the lattice of the basal plane was preferentially thinned along the zigzag direction terminated by an Mo- or S-edge. The orientation of the triangular pattern on the second top layer was 180° different than that on the top layer, but in alignment with that on the third layer, which implies that the stacking order is a hybrid of the 2H-MoS_2 and 3R-MoS_2 phases [53]. Finally, the MoS_2 demonstrated a defect-free hexagonal structure with a fringe lattice spacing of 0.27 nm away from the laser-treated region, but also exhibited a 2 nm thick amorphous region around the laser-treated region. The presence and size of the region was invariant with laser power. Altogether, the results suggest that laser thinning has great potential for selective and effective fabrication of high-quality MoS_2 devices with desired lateral dimensions and thicknesses. However, more work is required to further elucidate the role that the MoS_2 layers and substrate play in the thinning process. Particularly, different MoS_2 fabrication methods and substrates need to be investigated. In addition, the thermal behavior of the nanoparticles and their role in laser thinning needs to be more clearly identified. Furthermore, potential application areas for MoS_2 with controllable shape, size, and thickness need to be investigated. Nevertheless, the outcomes of this work provide useful insight into the laser thinning of MoS_2, and contribute to the development of laser thinning technologies for high-quality MoS_2 devices.

Acknowledgments

This research was supported by the Basic Science Research Program through the National Research Foundation of Korea (NRF), funded by the Ministry of Science, ICT and Future Planning (NRF-2017R1A2B4009651). Specific commercial equipment, instruments, and materials that are identified in this report are listed in order to adequately describe the experimental procedure and are not intended to imply endorsement or recommendation by the National Institute of Standards and Technology (NIST).

ORCID iDs

Frank W DelRio https://orcid.org/0000-0003-1727-8220
Koo-Hyun Chung https://orcid.org/0000-0002-9092-6784

References

[1] Feldman Y, Wasserman E, Srolovitz D J and Tenne R 1995 High-rate, gas-phase growth of MoS_2 nested inorganic fullerenes and nanotubes *Science* **267** 222–5

[2] Rapoport L, Bilik Y, Feldman Y, Homyonfer M, Cohen S R and Tenne R 1997 Hollow nanoparticles of WS_2 as potential solid-state lubricants *Nature* **387** 791–3

[3] Qian X, Liu J, Fu L and Li J 2014 Quantum spin Hall effect in two-dimensional transition metal dichalcogenides *Science* **346** 1344–7

[4] Manzeli S, Ovchinnikov D, Pasquier D, Yazyev O V and Kis A 2017 2D transition metal dichalcogenides *Nat. Rev. Mater.* **2** 17033

[5] Kuc A, Zibouche N and Heine T 2011 Influence of quantum confinement on the electronic structure of the transition metal sulfide TS_2 *Phys. Rev.* B **83** 245213

[6] Bertolazzi S, Brivio J and Kis A 2011 Stretching and breaking of ultrathin MoS_2 *ACS Nano* **5** 9703–9

[7] Lee C, Li Q, Kalb W, Liu X, Berger H, Carpick R W and Hone J 2010 Frictional characteristics of atomically thin sheets *Science* **328** 76–80

[8] Jariwala D, Sangwan V K, Lauhon L J, Marks T J and Hersam M C 2014 Emerging device applications for semiconducting two-dimensional transition metal dichalcogenides *ACS Nano* **8** 1102–20

[9] Wang T, Chen S, Pang H, Xue H and Yu Y 2017 MoS_2-based nanocomposites for electrochemical energy storage *Adv. Sci.* **4** 1600289

[10] Yadav V, Roy S, Singh P, Khan Z and Jaiswal A 2019 2D MoS_2-based nanomaterials for therapeutic, bioimaging, and biosensing applications *Small* **15** 1803706

[11] Wang Z and Mi B 2017 Environmental applications of 2D molybdenum disulfide (MoS_2) nanosheets *Environ. Sci. Technol.* **51** 8229–44

[12] Radisavljevic B, Radenovic A, Brivio J, Giacometti V and Kis A 2011 Single-layer MoS_2 transistors *Nat. Nano* **6** 147–50

[13] Britnell L *et al* 2012 Field-effect tunneling transistor based on vertical graphene heterostructures *Science* **335** 947–50

[14] Choi W *et al* 2012 High-detectivity multilayer MoS_2 phototransistors with spectral response from ultraviolet to infrared *Adv. Mater.* **24** 5832–6

[15] Fontana M, Deppe T, Boyd A K, Rinzan M, Liu A Y, Paranjape M and Barbara P 2013 Electron-hole transport and photovoltaic effect in gated MoS_2 Schottky junctions *Sci. Rep.* **3** 1634

[16] Late D J *et al* 2013 Sensing behavior of atomically thin-layered MoS_2 transistors *ACS Nano* **7** 4879–91

[17] Jiang H, Ren D, Wang H, Hu Y, Guo S, Yuan H, Hu P, Zhang L and Li C 2015 2D monolayer MoS_2–carbon interoverlapped superstructure: engineering ideal atomic interface for lithium ion storage *Adv. Mater.* **27** 3687–95

[18] Bang G S, Nam K W, Kim J Y, Shin J, Choi J W and Choi S 2014 Effective liquid-phase exfoliation and sodium ion battery application of MoS_2 nanosheets *ACS Appl. Mater. Interfaces* **6** 7084–9

[19] Acerce M, Voiry D and Chhowalla M 2015 Metallic 1T phase MoS_2 nanosheets as supercapacitor electrode materials *Nat. Nanotechnol.* **10** 313–8

[20] Chou S S, Kaehr B, Kim J, Foley B M, De M, Hopkins P E, Huang J, Brinker C J and Dravid V P 2013 Chemically exfoliated MoS_2 as near-infrared photothermal agents *Angew. Chem. Int. Ed.* **52** 4160–4

[21] Li B L, Setyawati M I, Chen L, Xie J, Ariga K, Lim C, Garaj S and Leong D T 2017 Directing assembly and disassembly of 2D MoS_2 nanosheets with DNA for drug delivery *ACS Appl. Mater. Interfaces* **9** 15286–96

[22] Kim J, Kim H and Kim W J 2016 Single-layered MoS_2–PEI–PEG nanocomposite-mediated gene delivery controlled by photo and redox stimuli *Small* **12** 1184–92

[23] Wu S, Zeng Z, He Q, Wang Z, Wang S J, Du Y, Yin Z, Sun X, Chen W and Zhang H 2012 Electrochemically reduced single-layer MoS_2 nanosheets: characterization, properties, and sensing applications *Small* **8** 2264–70

[24] Ai K, Ruan C, Shen M and Lu L 2016 MoS_2 nanosheets with widened interlayer spacing for high-efficiency removal of mercury in aquatic systems *Adv. Funct. Mater.* **26** 5542–9

[25] Midya A, Ghorai A, Mukherjee S, Maiti R and Ray S K 2016 Hydrothermal growth of few layer 2H-MoS_2 for heterojunction photodetector and visible light induced photocatalytic applications *J. Mater. Chem.* A **4** 4534–43

[26] Li W, Yang Y, Weber J K, Zhang G and Zhou R 2016 Tunable, strain-controlled nanoporous MoS_2 filter for water desalination *ACS Nano* **10** 1829–35

[27] Yang X, Li J, Liang T, Ma C, Zhang Y, Chen H, Hanagata N, Su H and Xu M 2014 Antibacterial activity of two-dimensional MoS_2 sheets *Nanoscale* **6** 10126–33

[28] Novoselov K S, Jiang D, Schedin F, Booth T J, Khotkevich V V, Morozov S V and Geim A K 2005 Two-dimensional atomic crystals *Proc. Natl Acad. Sci. USA* **102** 10451–3

[29] Coleman J N *et al* 2011 Two-dimensional nanosheets produced by liquid exfoliation of layered materials *Science* **331** 568–71

[30] Zeng Z, Yin Z, Huang X, Li H, He Q, Lu G, Boey F and Zhang H 2011 Single-layer semiconducting nanosheets: high-yield preparation and device fabrication *Angew. Chem. Int. Ed.* **50** 11093–7

[31] van der Zande A M, Huang P Y, Chenet D A, Berkelbach T C, You Y, Lee G, Heinz T F, Reichman D R, Muller D A and Hone J C 2013 Grains and grain boundaries in highly crystalline monolayer molybdenum disulphide *Nat. Mater.* **12** 554–61

[32] Wu J, Li H, Yin Z, Li H, Liu J, Cao X, Zhang Q and Zhang H 2013 Layer thinning and etching of mechanically exfoliated MoS_2 nanosheets by thermal annealing in air *Small* **9** 3314–9

[33] Lu X, Utama M I B, Zhang J, Zhao Y and Xiong Q 2013 Layer-by-layer thinning of MoS_2 by thermal annealing *Nanoscale* **5** 8904–8

[34] Liu Y, Nan H, Wu X, Pan W, Wang W, Bai J, Zhao W, Sun L, Wang X and Ni Z 2013 Layer-by-layer thinning of MoS_2 by plasma *ACS Nano* **7** 4202–9

[35] Huang Y *et al* 2013 An innovative way of etching MoS_2: characterization and mechanistic investigation *Nano Res.* **6** 200–7

[36] Castellanos-Gomez A, Barkelid M, Goossens A M, Calado V E, van der Zant H S J and Steele G A 2012 Laser-thinning of MoS_2: on demand generation of a single-layer semiconductor *Nano Lett.* **12** 3187–92

[37] Sunamura K, Page T R, Yoshida K, Yano T and Hayamizu Y 2016 Laser-induced electrochemical thinning of MoS_2 *J. Mater. Chem.* C **4** 3268–73

[38] Hu L, Shan X, Wu Y, Zhao J and Lu X 2017 Laser thinning and patterning of MoS_2 with layer-by-layer precision *Sci. Rep.* **7** 15538

[39] Tran Khac B C, Jeon K, Choi S T, Kim Y S, DelRio F W and Chung K 2016 Laser-induced particle adsorption on atomically thin MoS_2 *ACS Appl. Mater. Interfaces* **8** 2974–84

[40] Alrasheed A, Gorham J M, Tran Khac B C, Alsaffar F, DelRio F W, Chung K and Amer M R 2018 Surface properties of laser-treated molybdenum disulfide nanosheets for optoelectronic applications *ACS Appl. Mater. Interfaces* **10** 18104–12

[41] Yamamoto M, Einstein T L, Fuhrer M S and Cullen W G 2013 Anisotropic etching of atomically thin MoS_2 *J. Phys. Chem.* C **117** 25643–9
[42] Sener Sen H, Sahin H, Peeters F M and Durgun E 2014 Monolayers of MoS_2 as an oxidation protective nanocoating material *J. Appl. Phys.* **116** 083508
[43] Tran Khac B, DelRio F W and Chung K 2018 Interfacial strength and surface damage characteristics of atomically thin h-BN, MoS_2, and graphene *ACS Appl. Mater. Interfaces* **10** 9164–77
[44] Li H, Zhang Q, Yap C C R, Tay B K, Edwin T H T, Olivier A and Baillargeat D 2012 From bulk to monolayer MoS_2: evolution of Raman scattering *Adv. Funct. Mater.* **22** 1385–90
[45] Judek J, Gertych A P, Świniarski M, Łapińska A, Dużyńska A and Zdrojek M 2015 High accuracy determination of the thermal properties of supported 2D materials *Sci. Rep.* **5** 12422
[46] Bollinger M V, Jacobsen K W and Nørskov J K 2003 Atomic and electronic structure of MoS_2 nanoparticles *Phys. Rev.* B **67** 085410
[47] Helveg S, Lauritsen J V, Lægsgaard E, Stensgaard I, Nørskov J K, Clausen B S, Topsøe H and Besenbacher F 2000 Atomic-scale structure of single-layer MoS_2 nanoclusters *Phys. Rev. Lett.* **84** 951–4
[48] Moses P G, Hinnemann B, Topsøe H and Nørskov J K 2007 The hydrogenation and direct desulfurization reaction pathway in thiophene hydrodesulfurization over MoS_2 catalysts at realistic conditions: a density functional study *J. Catal.* **248** 188–203
[49] Beal A R, Knights J C and Liang W Y 1972 Transmission spectra of some transition metal dichalcogenides: II. Group VIA: trigonal prismatic coordination *J. Phys. C: Solid State Phys.* **5** 3540–51
[50] Wang Q H, Kalantar-Zadeh K, Kis A, Coleman J N and Strano M S 2012 Electronics and optoelectronics of two-dimensional transition metal dichalcogenides *Nat Nano* **7** 699–712
[51] Chhowalla M, Shin H S, Eda G, Li L, Loh K P and Zhang H 2013 The chemistry of two-dimensional layered transition metal dichalcogenide nanosheets *Nat. Chem.* **5** 263–75
[52] Han B and Hu Y H 2016 MoS_2 as a co-catalyst for photocatalytic hydrogen production from water *Energy Sci. Eng.* **4** 285–304
[53] Shinde S M, Dhakal K P, Chen X, Yun W S, Lee J, Kim H and Ahn J 2018 Stacking-controllable interlayer coupling and symmetric configuration of multilayered MoS_2 *NPG Asia Mater.* **10** e468
[54] Han G H *et al* 2011 Laser thinning for monolayer graphene formation: heat sink and interference effect *ACS Nano* **5** 263–8